JTTEE5 14:205-214
DOI: 10.1361/10599630523764
1059-9630/$19.00 © ASM International

An Analytical Model for Simulation of Heat Flow in Plasma-Sprayed Thermal Barrier Coatings

I.O. Golosnoy, S.A. Tsipas, and T.W. Clyne

(Submitted October 1, 2003; in revised form November 5, 2003)

Numerical (finite difference) and analytical models have been developed for the simulation of heat flow through plasma-sprayed coatings, allowing the effective thermal conductivity to be predicted as a function of microstructural parameters. The structure is assumed to be composed of lamellar material (splats), separated by (thin) pores, within which there are areas of contact (bridges). The analytical model is based on dividing the material into two regimes, within which the heat flow occurs either by unidirectional serial flow through lamellae and pores or by being funneled through the regions of the lamellae above and below the bridges. The validity of this model is demonstrated by a comparison of the predictions obtained from it and those obtained from the numerical model. The effects of pore geometry on conductive and radiative heat transfer within the coating have been investigated over a range of temperatures and gas pressures. It is shown that the main factor controlling the conductivity is the intersplat bridge area. Comparisons are also presented with experimental conductivity data, for cases in which some attempt has been made to characterize the key microstructural features. The study is oriented toward thermal barrier coatings, based on zirconia-yttria top coats. It is noted that the effect of microstructural sintering, which tends to occur in these coatings under service conditions, can be predicted using this model.

Keywords heat transfer, modeling, plasma spaying, thermal barrier coatings, thermal conductivity

1. Introduction

Thermal barrier coatings (TBCs) are central to development of the next generation of gas turbine aeroengines and are also important for power-generation turbines (Ref 1, 2). The current industry standard TBCs are based on zirconia-yttria top coats, which are produced by either plasma spraying or electron beam physical vapor deposition. The former are generally favored for power-generation turbines and the latter for aeroengines. A key objective for such applications is to maximize the temperature drop across the top coat, thus permitting higher turbine entry temperatures and hence higher engine efficiencies. This, in turn, requires that the thermal conductivity of the top coat should be minimized and also that the value should remain low during prolonged exposure to service conditions. It is becoming clear that, for the temperature ranges of interest, radiative heat transfer may be quite significant, and this should be taken into account when attempting to simulate the heat flow involved.

Plasma-sprayed zirconia tends to exhibit lower thermal conductivity values than vapor-deposited material, although there have been various attempts (Ref 3-8) to reduce the conductivities of both types. In both cases, the conductivity is thought to be dictated largely by microstructural features (Ref 7, 9, 10). In the case of plasma-sprayed material, the microstructure is essentially composed of an array of pancake-shaped splats, oriented parallel to the plane of the coating (normal to the heat flow direction), with relatively poor intersplat contact. An example is shown in Fig. 1(a). Vapor-deposited material, on the other hand, is composed of poorly connected columnar structures oriented parallel to the heat flow direction. This leads to higher through-thickness conductivity, although it also confers a lower in-plane stiffness and hence a superior strain tolerance. There is in both cases a concern (Ref 11-15) that prolonged exposure to high temperatures may change the microstructure in such a way as to raise the thermal conductivity, and also to make the material stiffer and more prone to spallation. An illustration of the kind of microstructural change that occurs can be seen in Fig. 1(b).

Numerous models were developed for the simulation of the heat flow through various types of composite and porous material. Attention is focused here on two-phase systems in which the second phase is in the form of gas-filled pores. Such systems can be modeled as incorporating randomly distributed pores (Ref 10, 16-18), contact resistance (Ref 19-21), or periodic structures (Ref 6, 22). Randomly distributed inclusions, at dilute concentrations, were modeled under the assumption that they are noninteracting (Ref 10, 17), whereas for higher porosity levels self-consistent models (Ref 23, 24) and effective medium models (Ref 16, 25) were developed. The latter considers the need for an isolated inclusion to be placed into the material with an effective conductivity that differs from that of the real matrix.

Several models were developed specifically for plasma-sprayed coatings and other layered systems, which are believed to be composed of arrays of solid lamellae with small contact areas between them. McPherson (Ref 19) assumed that two independent heat fluxes would arise in such a system, one through

I.O. Golosnoy, S.A. Tsipas, and **T.W. Clyne,** Department of Materials Science & Metallurgy, Cambridge University, Pembroke Street, Cambridge CB2 3QZ, UK. Contact e-mail: twc10@cam.ac.uk.

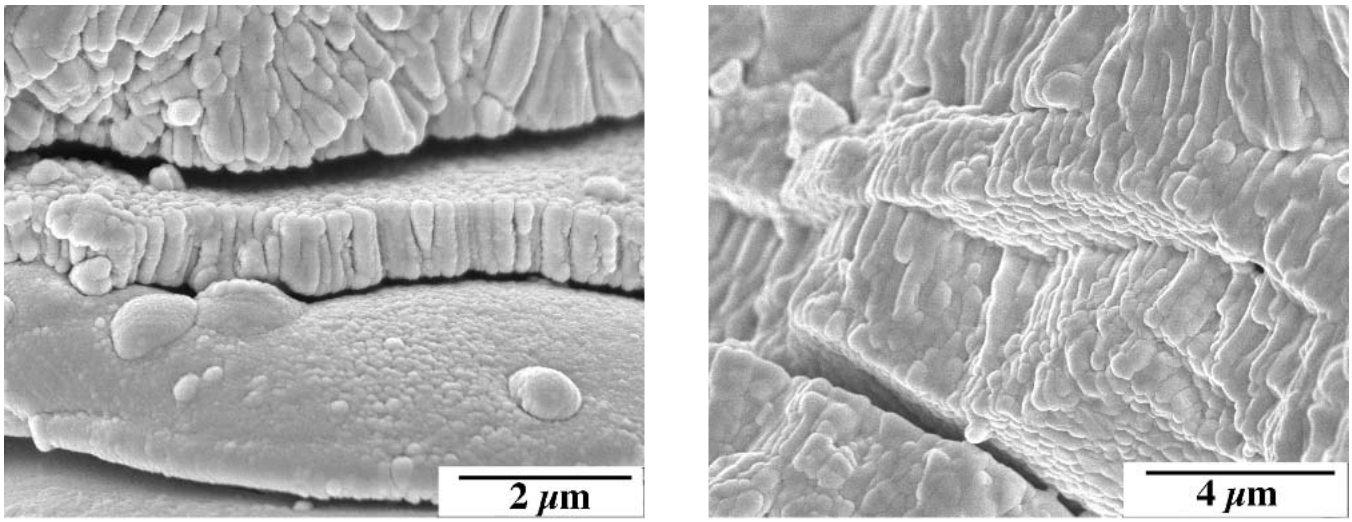

Fig. 1 Fracture surfaces from plasma-sprayed zirconia-7% yttria coatings: (a) as-sprayed; and (b) after a heat treatment of 50 h at 1300 °C

Nomenclature

α	m^{-1}	extinction coefficient
β	m^{-1}	scattering coefficient
κ	m^{-1}	absorption coefficient
λ	m	mean free path of the gas molecules
δ	m	penetration depth
σ_{SB}	$W\ m^{-2}\ K^{-4}$	Stefan-Boltzmann constant
B	$Pa\ m\ K^{-1}$	constant
c	$J\ m^{-3}\ K^{-1}$	volume specific heat
d_v	m	pore thickness
d	m	pore length between bridges
f_p		volume fraction of inter-splat porosity
k	$W\ m^{-1}\ K^{-1}$	local thermal conductivity in the unit cell
k_0	$W\ m^{-1}\ K^{-1}$	total conductivity of lamellae
k_1, k_2	$W\ m^{-1}\ K^{-1}$	conductivities of two regions in TFR model
k_{br}	$W\ m^{-1}\ K^{-1}$	effective conductivity of bridge
k_p	$W\ m^{-1}\ K^{-1}$	total conductivity of pore
k_{rad}	$W\ m^{-1}\ K^{-1}$	radiative conductivity
k_g	$W\ m^{-1}\ K^{-1}$	collosion conductivity of gas in a pore (with dimension <~λ)
k_g^0	$W\ m^{-1}\ K^{-1}$	normal collision conductivity of gas
k_{eff}	$W\ m^{-1}\ K^{-1}$	effective conductivity of the material
L_v	m	height of the unit cell
L_h	m	width of the unit cell
n		refractive index
P	Pa	gas pressure
S	m^2	area of the "contact" region in TFR model
S_{br}	m^2	cross-section area of bridge
S_{tot}	m^2	total cross-section area of unit cell
T	K	temperature
T_u	K	temperature at upper surface of unit cell
T_d	K	temperature at lower surface of unit cell
x, y, z	m	local coordinates

the contact areas and the other through the pores. He ascribed a thermal resistance to the contact regions. The thermal resistance of the lamellae (Ref 20) and the oxidation of the contact areas (Ref 21) have also been incorporated into such models, with heat flow through the pores being ignored. The original two-dimensional (2D) shear lag analysis of Lu and Hutchinson (Ref 22), which was designed for cross-ply composites with matrix cracks, has since been extended to TBCs by Lu et al. (Ref 6), treating them as exhibiting a 2D periodic structure of thin cracks in a uniform matrix.

In the present article, a relatively simple analytical model is presented for the prediction of the thermal conductivity of a layered two-phase structure, which is intended to be representative of plasma-sprayed coatings, with and without radiative contributions. Comparisons are presented between predictions from this model and those from a numerical simulation. Some experimental conductivity measurements are also considered, in conjunction with relevant microstructural characterization data, although such correlated information is unfortunately in very short supply.

2. Modeling of Heat Transfer

2.1 Pore Geometry

Because plasma-sprayed TBC microstructures are essentially made up of high-aspect-ratio splats, with relatively poor contact between the splats (Fig. 1), a model was set up comprising a periodic array of lamellae, separated by pores, with bridges between them. To explore the influence of key geometrical parameters, the pores in successive layers were assumed to be in either aligned or staggered arrangements, as depicted in Fig. 2. The lamellae themselves might incorporate different heterogeneous inclusions, such as equiaxed pores or vertical cracks, as well as grain boundaries. These would affect the average thermal conductivity of the lamellae, which could thus differ from that of fully dense solid material.

Two types of structure are explored, corresponding to open or closed porosity distributions (Fig. 3). The top and bottom surfaces of the unit cell are taken as midplanes of neighboring splats, and the pores at midplane of the unit cell represent the intersplat regions. Both cases are characterized by six parameters (four geometrical and two physical). The geometrical parameters are the height (L_v) and thickness (L_h) of the unit cell, the thickness of the pore (d_v), and an interbridge (or interpore) distance (d). There are two conductivities, k_0 (lamellar material) and k_p (pore). These conductivities are not necessarily just those of the material occupying the regions concerned, but could incorporate radiative contributions and, for the case of the gas in the pores, the effect of pore dimensions (if the molecular mean free path is similar in size to these or larger). The normalized thermal conductivity of the material as a whole (k_{eff}/k_0) is a function of only three geometrical parameters (the normalized bridge area $[1 - d/L_h]^2$; the normalized interbridge distance L_h/L_v; and the normalized bridge height d_v/L_v) and one physical parameter (the normalized thermal conductivity of a pore k_p/k_0).

2.2 Physical Assumptions

The heat flux within each constituent can be split into two parts: conventional phonon conduction through a polycrystalline solid (or collision conductivity in the gas); and radiative heat

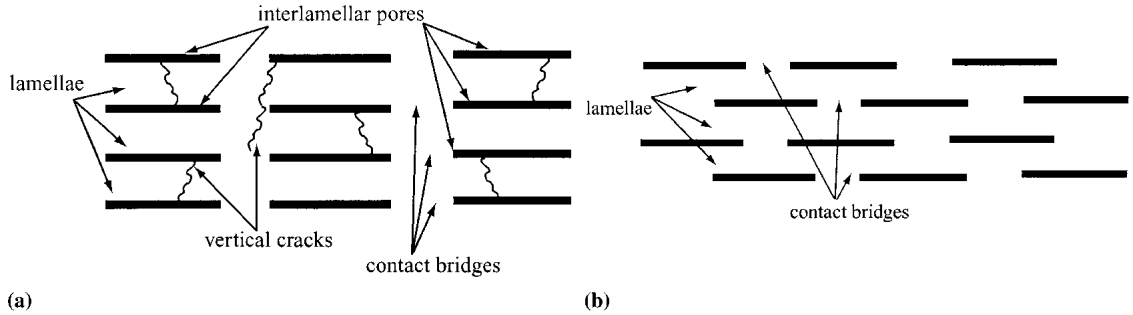

Fig. 2 Modeled periodic lamellar structures, showing (a) aligned and (b) staggered pore configurations

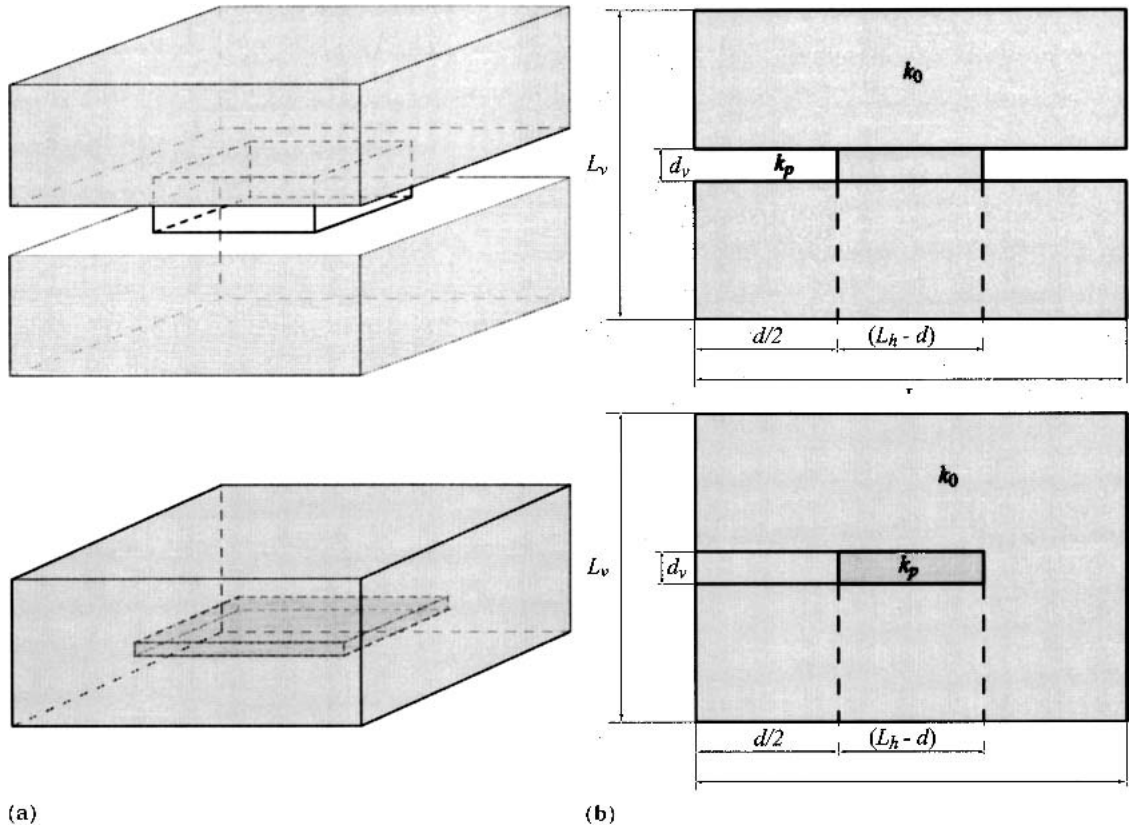

Fig. 3 Modeled unit cells, for (top) open porosity (isolated bridges) and (bottom) closed porosity, showing (a) perspective views and (b) vertical sections

transfer through translucent material. There are no free electrons in the constituents being considered.

2.2.1. Phonon Conductivity in the Solid Constituent. The thermal conductivity of dense yttria-stabilized zirconia has been measured (Ref 26) at high temperatures, as a function of the crystal structure and the concentration of stabilizing dopants. The effect of dopant level on the conductivity is quite strong. The current study is oriented toward tetragonal zirconia, partially stabilized by 8 wt.% yttria. For this material, the thermal conductivity depends only weakly on temperature over the range of interest and has a value (Ref 26, 27) of about 2.25 W m^{-1} K^{-1}.

2.2.2 Molecular Collision Conduction Through Gas in the Pores. The gas in the pores can also conduct heat. Because the pore thickness, d_v, is comparable to the mean free path of molecules in a typical gas at atmospheric pressure (λ ~100 nm), convection can be neglected, and the thermal conductivity of the gas, k_g, can be estimated using a simple analytical expression (Ref 28):

$$k_g = \frac{k_g^0}{1 + B\,T/(d_v P)} \qquad \text{(Eq 1)}$$

where k_g^0 is the normal conductivity of the gas at the temperature concerned, P is the pressure, T is the temperature (in degrees K), and B is a constant, with a value of 2.5 10^{-5} Pa m K^{-1} for air. There are analytical expressions available for k_g^0 as a function of temperature, but in practice significant deviations are common and experimental data should be used. For example, Fig. 4(a) shows measured values for k_g^0 of air (Ref 29), together with calculated values of k_g for different pore thicknesses and gas pressures. It can be seen that both pore thickness and gas pressure can have significant effects on the pore conductivity, as well as the temperature.

In noting the effect of gas pressure, it may be recalled that in the hot end of a typical gas turbine engine, the pressure varies between about 40 atm and 1 atm. Furthermore, the gas permeability of TBC top coats is known (Ref 30) to be very high, so such pressures will quickly become established throughout most of the pores within such coatings. However, experimental measurements of thermal conductivity are normally carried out either at 1 atm or under reduced pressure (higher λ), in which case the pore conductivity will be appreciably lower. Furthermore, measurements are often made at room temperature, which will also have the effect of reducing the pore conductivity. For example, at T = 300 K and p = 0.01 atm the conductivity of air is 8 10^{-5} W m^{-1} K^{-1}. This value has thus been used for modeling of the low-temperature case (i.e., with no radiative contribution).

2.2.3 Radiative Heat Transfer. Depending on the temperature, radiative heat transfer may be significant in gases and translucent solids. If the radiation penetration depth is much greater than the lamellar thickness, then pores become active scattering centers (Ref 31, 32) as well as grain boundaries. The dependence of the scattering coefficient on porosity is thus expected to be quite strong, particularly in lamellar materials, and several methods have been developed (Ref 33) to infer changes in porosity level from measured changes in transmittance. In the present case, there is an approximately uniform radiation flux through the material, but pores change the scattering characteristics, decreasing the penetration depth relative to that in a fully dense material. Porosity at a level of a few percent may thus induce a change of an order of magnitude in the scattering coefficient (Ref 31, 33).

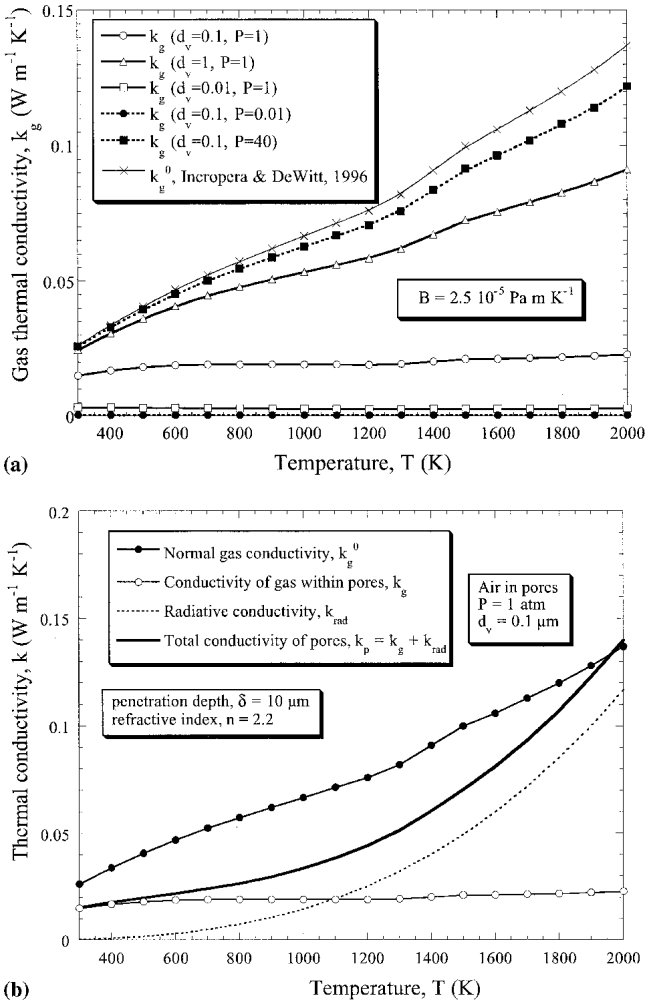

Fig. 4 Dependence on temperature of the contributions to the thermal conductivity of the pores, showing (a) effects of pore thickness and gas pressure on the conductivity of air (Ref 29), according to Eq 1, and (b) radiative and conductive contributions to the overall pore conductivity, for air at atmospheric pressure with a pore thickness of 0.1 μm, according to Eq 2

The conventional approach to the simulation of the radiative contribution to the heat transfer in such materials is to introduce a radiative conductivity (Ref 31, 34), which is additive to that for conduction,

$$k_{rad} \approx \frac{16n^2}{3\alpha}\,\sigma_{SB} T^3 \qquad \text{(Eq 2)}$$

in which σ_{SB} is the Stefan-Boltzmann constant and n is the refractive index. The parameter α (= β + κ) is an extinction coefficient, which is made up of scattering (β) and absorption (κ) coefficients. Scattering tends to dominate for typical TBC materials (zirconia and alumina) (Ref 35), so that $\alpha \approx \beta$. In using this formulation, uniform radiation scattering is assumed, and any

wavelength dependence or boundary effects are neglected. It is common to express the behavior in terms of a penetration depth, given by:

$$\delta = \frac{1}{\alpha} \quad \text{(Eq 3)}$$

which is a characteristic decay distance, over which the intensity of the radiation will fall by a factor of 1/e. (However, it should be noted that there may be multiple scattering events, such that much of the scattered radiation will in fact penetrate deeper into the material: the exponential decay refers to unscattered radiation.) It is assumed that Eq 2 can be used for radiative contributions both in the solid constituent and in the pores.

The penetration depth for TBCs is expected to be lower than that for sintered zirconia, which has been reported (Ref 35, 36) to be about 50 μm. Some relevant data are available (Ref 31, 32, 37) for alumina, in the form of refractive indices and penetration depths for material with different porosity levels and degrees of cracking. From this information, it may be deduced that appropriate values of δ and n for plasma-sprayed zirconia are on the order of 10 μm and 2.2, respectively. Using these figures, the conductive and radiative contributions to the effective pore conductivity, as a function of temperature, are shown in Fig. 4(b) for a pore thickness of 0.1 μm and a gas pressure of 1 atm. It can be seen that the radiative contribution to the pore conductivity starts to become substantial for temperatures above about 1000 K. For a representative elevated temperature of 1500 K, the value of k_{rad} is about 0.05 W m^{-1} K^{-1}. This would be raised by a factor of 5 if the penetration depth were to be increased from 10 to 50 μm, whereas the conductive contribution would be raised by a factor of ~2 if the gas pressure were to be increased to 40 atm. If the pore thickness were to be doubled, the conductive contribution would rise by something like 10 to 20%. Because n is unlikely to vary very much (Ref 38), the sensitivity to this parameter is of less concern.

3. Three-Dimensional Numerical Model

3.1 Mesh Structure and Finite Difference Approximation

The basic model relates to the aligned structure (Fig. 2a). The unit cell is a parallelepiped. The modeled volume incorporates the main microstructural features. Appropriate dimensions (Fig. 1) might be a typical splat thickness of about 2 μm and an interbridge distance of about 4 to 8 μm. A three-dimensional cartesian mesh with uniform spacing was superimposed on the cell, with approximately 100 volume elements in each direction, giving a total of about 10^6. The steady-state temperature distribution was obtained by a relaxation of transient heat transfer equation (Ref 39, 40):

$$c\frac{\partial T}{\partial t} = \text{div}(k \text{ grad } T) \quad \text{(Eq 4)}$$

where c is the volume specific heat. The temperature dependence of the thermal conductivity k has been neglected in most of the current work, except that values have been used corresponding to low-temperature (~300 K) and high-temperature (~1500 K) regimes. The focus here is mainly on the influence of geometric and microstructural factors. The evolving temperature distribution was obtained using an implicit method based on the alternating direction implicit (ADI) technique (Ref 39, 40), with a 1% convergence criterion.

3.2 Boundary Conditions and Input Data

It was assumed that the temperatures were fixed on the upper $T(x, y, 0) = T_u$ and lower $T(x, y, L_v) = T_d$ surfaces, and that no lateral heat exchange occurred between the cell and its surroundings:

$$\left.\frac{\partial T}{\partial x}\right|_{side} = \left.\frac{\partial T}{\partial y}\right|_{side} = 0 \quad \text{(Eq 5)}$$

The initial temperature distribution was uniform throughout the cell and was set equal to $0.5(T_u + T_d)$.

The main input parameters concerning geometry are the splat thickness ($= L_v - d_v$), intersplat bridge area (S_{br}/S_{tot}), intersplat pore thickness, (d_v) and the intersplat pore volume fraction (f_p), which determines the bridge spacing, L_h. These values can be inferred from various types of experimental measurements, including the inspection of micrographs, densitometry, and small angle neutron scattering (SANS). The SANS technique (Ref 41-44) gives information about the spacings between planes, which act as strong scattering centers, such as splat surfaces.

In general, splat thickness depends only weakly on spraying conditions and sprayed material (Ref 45-47): a typical value for sprayed zirconia would be about 2 μm, and this figure was used in the present work. A reference value used for the intersplat pore thickness was 0.2 μm, which is consistent with evidence from microscopy (Ref 48) and SANS (Ref 41-44) for sprayed zirconia. From densitometry and SANS data, the intersplat pore volume fraction can be estimated to be ~3%. The relationships among the bridge area, pore volume fraction, splat thickness, and intersplat pore thickness can be expressed:

$$\frac{S_{br}}{S_{tot}} = 1 - \frac{L_v f_p}{d_v} \quad \text{(Eq 6)}$$

In practice, the bridge area and the interbridge spacing might vary over quite a range, particularly as a consequence of post-deposition sintering effects, so the effects of altering these parameters were investigated. Typical initial values (Ref 48) might be 10 to 30% and 5 to 10 μm, respectively.

3.3 Predicted Effects of Pore Geometry

A comparison between predictions for isolated bridges (open porosity) and for isolated pores (closed porosity) for a given contact area is shown in Fig. 5(a) for the case of a negligible radiative contribution (T ~300 K). It can be seen that the conductivity is slightly lower, with open porosity in the range of contact areas up to about 40%, above which the differences are small. Attention can thus be focused on the open-porosity case, which probably best reflects the actual geometry of the intersplat regions in plasma-sprayed material, while recognizing that the closed po-

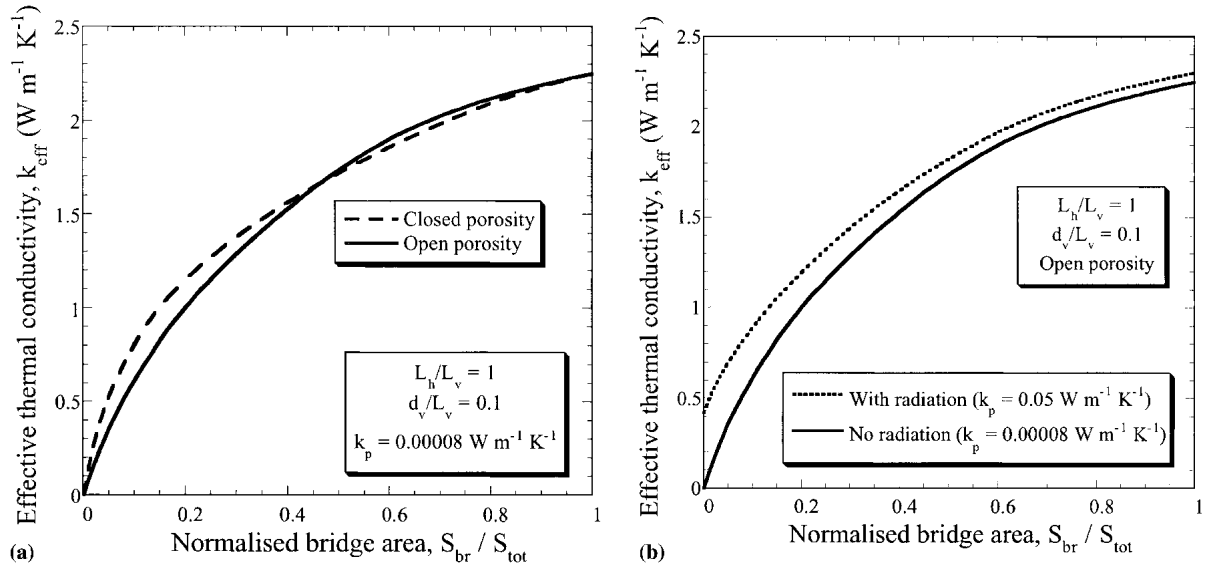

Fig. 5 Effective thermal conductivity as a function of bridge area, as predicted using the numerical model, showing the effects of (a) pore geometry and (b) the contribution from radiation (for T = 1500 K, p = 1 atm and d_v = 0.1 μm)

rosity case would give similar predictions. Figure 5(b) shows that the incorporation of a radiative component in the pore conductivity (representative of behavior at a temperature of ~1500 K) has a significant effect on the overall conductivity. For example, with a contact area of 10 to 20%, which might be typical of as-sprayed material, radiation is predicted to raise the overall effective conductivity by about 20 to 30% at this temperature.

The effect of microstructural regularity is shown in Fig. 6. It can be seen that the predicted conductivity is lower when the bridges between layers are offset from each other, rather than lined up. This is unsurprising, because the heat conduction path through the solid will be longer when the unit cells are staggered in this way (Fig. 2). The effect is stronger at higher bridge spacings. It is expected to be less noticeable when there is a smaller difference between the conductivity of the solid and that of the pore, and in this way the introduction of a radiative contribution leads to a reduced effect.

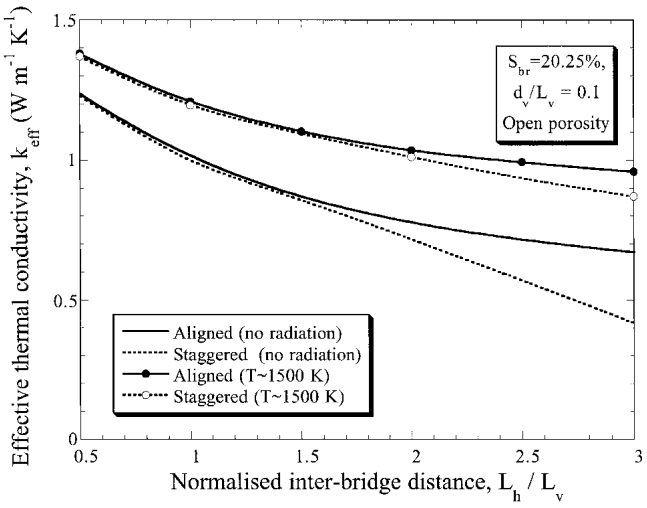

Fig. 6 Effective thermal conductivity as a function of normalized interbridge distance, as predicted using the numerical model, showing the effects of bridge alignment between a cell and the cells above and below (Fig. 2), and of having a radiative contribution, which raises the effective pore conductivity

4. Two-Flux Regions Analytical Model

4.1 Formulation of the Model

The unit cell is divided into two regions, as illustrated in Fig. 7. In the first zone, which includes the bridge, heat flow is assumed to take place only through the solid material. The effective conductivity of this zone depends on the area S. The second region contains two layers of solid material and the pore between them. The sizes of these regions are not known a priori. They can be established by maximizing the conductance of the assemblage. The fluxes in the two regimes are assumed to be independent, so that:

$$k_{\text{eff}}(S) = \frac{S}{S_{\text{tot}}} k_1(S) + \frac{S_{\text{tot}} - S}{S_{\text{tot}}} k_2 \qquad \text{(Eq 7)}$$

where $k_1(S)$ and k_2 are the conductivities of the two regions. The condition required can be expressed:

$$k_{\text{eff}} = \max_{S \in [S_{\text{br}},\, S_{\text{tot}}]} k_{\text{eff}}(S) \qquad \text{(Eq 8)}$$

To find k_{eff}, k_1 must be modeled as a function of the size of the region (area S), because k_2 is independent of S and is given by a standard series addition expression:

$$k_2 = \left(\left\{ 1 - \frac{d_v}{L_v} \right\} \frac{1}{k_0} + \frac{d_v}{L_v} \frac{1}{k_p} \right)^{-1} \qquad \text{(Eq 9)}$$

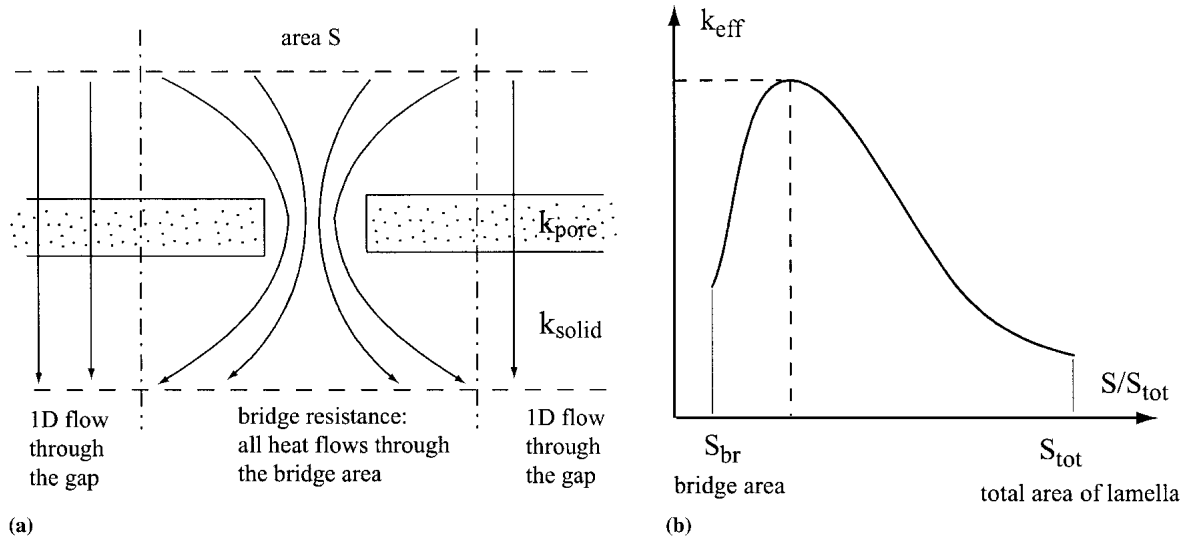

Fig. 7 Schematic depiction of the TFRs model, showing (a) heat flow paths and (b) a plot of how the effective conductivity varies with the area S, through which the heat flux is funneled in the vicinity of a bridge

The total conductivity of the contact region k_1 contains two terms. The first is the effective conductivity of the bridge itself:

$$k_{br} = \frac{S_{br}}{S} k_0 \qquad \text{(Eq 10)}$$

The second term is the effective conductivity of the region within which the heat flow is being funneled toward (or away from) the bridge. This is usually referred to as a contact resistance, emphasizing that it is the value for the resistivity of an infinitesimally thin bridge. Contact resistances of this type have been investigated in several articles (Ref 6, 19-22). At the limit of a small contact area ($d \sim L_h$) it is given by (Ref 19, 20):

$$k_{res} = k_0 \left(1 + \frac{\sqrt{\pi} L_h^2}{2(L_h - d)L_v} \right)^{-1} \qquad \text{(Eq 11)}$$

whereas for a large contact ($d << L_h$) a modified shear-lag method gives (Ref 6, 22):

$$k_{res} = k_0 \left(1 + \frac{d^{3/2}(2L_h - d)^{3/2}}{2^{3/2}(L_h - d)L_h L_v} \right)^{-1} \qquad \text{(Eq 12)}$$

A simple interpolation process between Eq 11 and 12 was carried out to give the contact resistance as a function of the region surface and bridge (contact) areas:

$$k_{res}(S) = k_0 \left(1 + \frac{\sqrt{\pi}}{2[1 + \sqrt{2\pi} S_{br}/S]} \left\{ \frac{S - S_{br}}{S} \right\}^{3/2} \frac{S}{L_v S_{br}^{1/2}} \right)^{-1} \qquad \text{(Eq 13)}$$

Then the conductivity of the first region is given by a simple series addition expression:

$$k_1(S) = \left(\left\{ 1 - \frac{d_v}{L_v} \right\} \frac{1}{k_{res}(S)} + \frac{d_v}{L_v} \frac{S}{S_{br} k_0} \right)^{-1} \qquad \text{(Eq 14)}$$

Equation 8 can thus be solved. The maximum occurs either at some intermediate value of the fractional bridge area or at the total bridging limit ($S_{br} = S_{tot}$). This is illustrated by the plots shown in Fig. 8.

4.2 Comparison With Predictions From Other Models

A comparison is shown in Fig. 9 of predictions from the numerical model, the two-flux regions (TFRs) model, and two other analytical models, using typical input data for a TBC, in the absence of radiation. (Radiative contributions have not been incorporated into the two models from previous work.) It can be seen that the TFRs model is in good agreement with the numerical modeling predictions, while the other two can lead to some substantial errors, depending on the regimes of bridge area and interbridge distance that are concerned. This arises from certain simplifications and approximations incorporated in them.

4.3 Comparison With Experimental Data

Unfortunately, while there are many reported thermal conductivity measurements for plasma-sprayed TBCs, there are certain problems in making comparisons with predictions from microstructure-based models. In particular, the properties of plasma-sprayed TBCs are often very sensitive to powder composition and spraying conditions (Ref 41, 44), so it is important that both thermal properties and microstructural features should be measured on the same specimens. There have been very few systematic studies of this type. Furthermore, there are difficulties in making reliable measurements of microstructural features such as intersplat bridge areas and spacings. These are often more clearly seen on fracture surfaces, such as those shown in

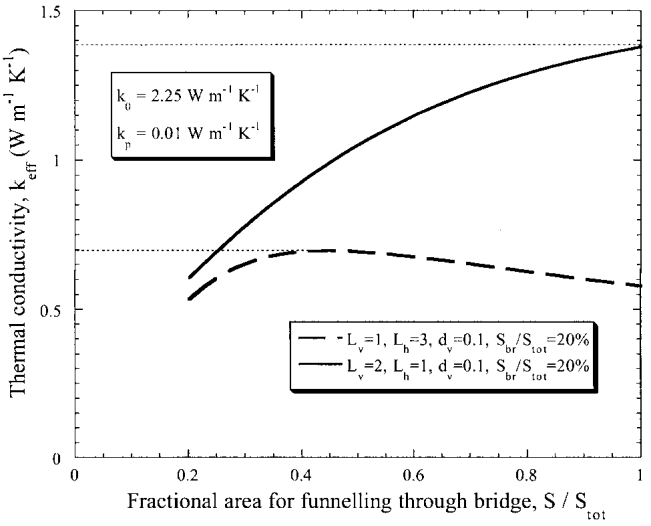

Fig. 8 Plot of effective thermal conductivity against fractional funneling area, for two cases, illustrating how this parameter is chosen in the TFRs model so as to maximize the net heat flux, and hence the conductivity

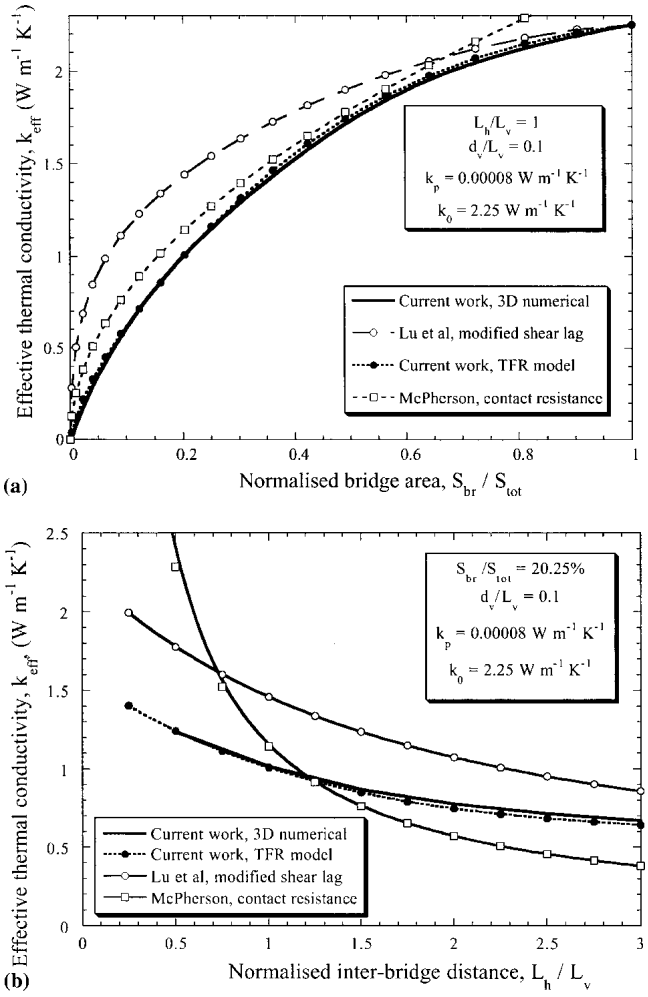

Fig. 9 Effective conductivity for different models, with no radiative contribution, as a function of (a) bridge area and (b) interbridge distance

Fig. 1, rather than on polished sections, but it is possible that the microstructure could be affected by the fracturing process. However, there have been a few studies in which systematic measurements have been made of both conductivity and microstructural parameters. Data from one such study (Ref 43) are presented in Fig. 10. It can be seen that the substitution of appropriate input data into the TFRs model gives predictions for the thermal conductivity that are consistent with these measurements. For these particular input data, the predictions of the McPherson (Ref 19) model look rather unreliable, while those of Lu et al. (Ref 6) are closer to the experimental data and to the data from the TFRs model.

It is also possible to explore how the TFRs model can be used to study the effects of progressive changes in microstructure. An example is shown in Fig. 11, which shows some experimental data (Ref 49) for the changing thermal conductivity (measured in situ at high temperature) during extended heat treatment, with the top coat held between about 1100 and 1300 °C. It can be seen that, over a period of about 20 h, the conductivity rose by about 40% (from 1 to 1.4 W m^{-1} K^{-1}). Also shown in this figure is the corresponding bridge area, obtained using the TFRs model, assuming that the other microstructural parameters (shown in the figure) remained constant during the heat treatment. This plot suggests that the bridge area rose from about 20% to just over 40% during this period. While this procedure is clearly an approximate one, this plot gives at least some idea of how the operation of the sintering mechanisms generates microstructural changes, which affect the coating conductivity.

5. Conclusions

The following conclusions can be drawn from this work.

- Analytical and numerical models have been set up for the simulation of heat flow through two-constituent structures (comprising solid layers separated by thin, periodically bridged, gas-filled voids), which were designed to be representative of plasma-sprayed ceramic coatings. This heat flow includes phonon conduction through the solid constituent, molecular collision conduction through the gas in the pores, and radiative heat transfer through both constituents. The effective thermal conductivity of the coating material has thus been predicted as a function of microstructural parameters and operating conditions.
- The analytical model, termed the TFRs model, is based on a division of the modeled domain into two regions, one characterized by serial heat flow through solids and pores, and the other by channeled conduction through the bridges. The implementation of the model is straightforward and can be carried out via a simple spreadsheet operation. It has been demonstrated, by comparison with predictions from the numerical model, that the TFRs model gives accurate predictions of the effective conductivity over a wide range of geometrical and physical boundary conditions. In this respect, the model appears to be more reliable than previously published analytical models that were designed to simulate heat flow through this type of material.

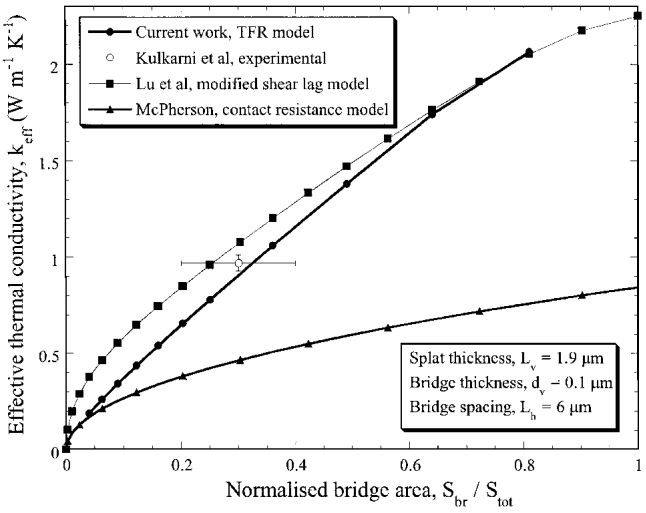

Fig. 10 Comparison between predicted conductivities obtained from the different models and from the experimental data of Kulkarni et al. (Ref 43)

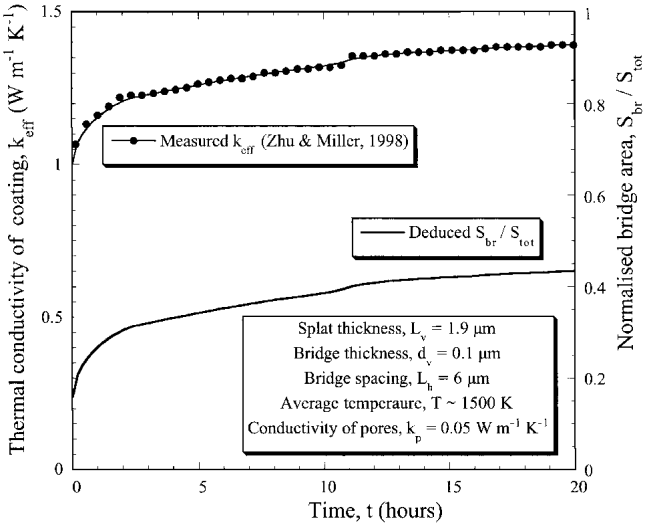

Fig. 11 Experimental data (Ref 49) for the thermal conductivity of a plasma-sprayed zirconia coating, measured at high temperature on a specimen being subjected to prolonged heat treatment in a thermal gradient (at an average temperature of ~1200 °C). Also shown is a plot of the corresponding intersplat bridge area, which was deduced from the TFRs model using the input data shown in the figure.

- It has been shown that, in general, the sensitivity of the predicted thermal conductivity to the model geometry (e.g., whether the interlayer porosity is open or closed, and whether bridge regions in neighboring unit cells are aligned with each other) is relatively small. The microstructural parameter predicted to have the strongest effect on the conductivity is the bridge area.
- The contribution of radiative heat transfer to the effective pore conductivity is predicted to become substantial for temperatures above ~1000 K. The significance of radiative heat transfer for the overall effective conductivity depends on the bridge area, but, for values thought to be typical of as-sprayed material, it is predicted that radiation becomes important at temperatures above ~1300 to 1500 K. Because service temperatures for TBCs are currently being pushed up to this range and beyond, it is clear that radiative heat transfer must be incorporated in both measurement and modeling activities.
- Higher gas pressures in the pores, up to the range typical of gas turbine service conditions, can significantly raise the pore conductivity, particularly at relatively high temperatures. Conversely, the pore conductivity is predicted to be low under reduced pressure, which is sometimes used for experimental measurements. Depending on the temperature and microstructure, there may be a significant effect on the overall conductivity.
- Some limited comparisons have been made between experimentally measured conductivities and predictions from the TFRs model. These suggest that it should be possible to predict the conductivity from measurable microstructural parameters. Furthermore, conductivity data obtained during extended heat treatment have been used to infer the microstructural changes caused by the associated sintering phenomena.

Acknowledgments

Funding for this work came from Engineering and Physical Sciences Research Council (EPSRC), in the form of a Platform Grant and a research project, which has had Rolls Royce and Sulzer as industrial partners. The authors are grateful to Dr. Rajiv Damani, of Sulzer Innotec, and Keith Harrison, Clive Britton, Jason Doesburg, and Andrew Nicoll, of Sulzer, for ongoing participation and support. The collaboration of Prof. Richard Jones, from Defence Science Technology Laboratory (DSTL), has also been very helpful.

References

1. R.A. Miller, Thermal Barrier Coatings for Aircraft Engines: History and Directions, *J. Thermal Spray Technol.,* Vol 6, 1997, p 35-42
2. W. Beele, G. Marijnissen, and A. van Lieshout, The Evolution of Thermal Barrier Coatings: Status and Upcoming Solutions for Today's Key Issues, *Surf. Coat. Technol.,* Vol 121, 1999, p 61-67
3. R. Hamacha, P. Fauchais, and F. Nardou, Influence of Dopant on the Thermal Properties of Two Plasma-sprayed Zirconia Coatings: 1. Relationship Between Powder Characteristics and Coating Properties, *J Thermal Spray Technol.,* Vol 5, 1996, p 431-438
4. J.R. Nicholls, K.J. Lawson, A. Johnstone, and D.S. Rickerby, Low Thermal Conductivity EB-PVD Thermal Barrier Coatings, *Mater. Sci. Forum,* Vol 369-372, 2001, p 595-606
5. S. Gu, T.J. Lu, D.D. Hass, and H.N.G. Wadley, Thermal Conductivity of Zirconia Coatings with Zig-Zag Pore Microstructures, *Acta Mater.,* Vol 49, 2001, p 2539-2547
6. T.J. Lu, C.G. Levi, H.N.G. Wadley, and A.G. Evans, Distributed Porosity as a Control Parameter for Oxide Thermal Barriers Made by Physical Vapor Deposition, *J. Am. Ceram. Soc.,* Vol 84, 2001, p 2937-2946
7. K.W. Schlichting, N.P. Padture, and P.G. Klemens, Thermal Conductivity of Dense and Porous Yttria-Stabilized Zirconia, *J. Mater. Sci.,* Vol 36, 2001, p 3003-3010
8. J.R. Nicholls, K.J. Lawson, A. Johnstone, and D.S. Rickerby, Methods to Reduce the Thermal Conductivity of EB-PVD TBCs, *Surf. Coat. Technol.,* Vol 151, 2002, p 383-391
9. S. Orain, Y. Scudeller, and T. Brousse, Structural and Microstructural

Effects on the Thermal Conductivity of Zirconia Thin Films, *Microscale Thermophys. Eng.,* Vol 5, 2001, p 267-275
10. I. Sevostianov and M. Kachanov, Anisotropic Thermal Conductivities of Plasma-Sprayed Thermal Barrier Coatings in Relation to the Microstructure, *J. Thermal Spray Technol.,* Vol 9, 2000, p 478-482
11. P.A. Langhahr, R. Oberacker, and M.J. Hoffmann, Long-Term Behaviour and Application Limits of Plasma-Sprayed Zirconia Thermal Barrier Coatings, *J. Am. Ceram. Soc.,* Vol 84, 2001, p 1301-1208
12. D.M. Zhu and R.A. Miller, Thermal Conductivity and Elastic Modulus Evolution of Thermal Barrier Coatings under High Heat Flux Conditions, *J. Thermal Spray Technol.,* Vol 9, 2000, p 175-180
13. R. Dutton, R. Wheeler, K.S. Ravichandran, and K. An, Effect of Heat Treatment on the Thermal Conductivity of Plasma-Sprayed Thermal Barrier Coatings, *J. Thermal Spray Technol.,* Vol 9, 2000, p 204-209
14. D. Basu, C. Funke, and R.W. Steinbrech, Effect of Heat Treatment on Elastic Properties of Separated Thermal Barrier Coatings, *J. Mater. Res.,* Vol 14, 1999, p 4643-4650
15. J.A. Thompson and T.W. Clyne, The Effect of Heat Treatment on the Stiffness of Zirconia Top Coats in Plasma-Sprayed TBCs, *Acta Mater.,* Vol 49, 2001, p 1565-1575
16. T.W. Clyne and P.J. Withers, *An Introduction to Metal Matrix Composites,* Cambridge University Press, Cambridge, UK, 1993
17. B. Shafiro and M. Kachanov, Anisotropic Effective Conductivity of Materials with Nonrandomly Oriented Inclusions of Diverse Ellipsoidal Shapes, *J. Appl. Phys.,* Vol 87, 2000, p 8561-8569
18. F. Cernuschi, P. Bianchi, M. Leoni, and P. Scardi, Thermal Diffusivity/Microstructure Relationship in Y-PSZ Thermal Barrier Coatings, *J. Thermal Spray Technol.,* Vol 8, 1999, p 102-109
19. R. McPherson, A Model for the Thermal Conductivity of Plasma-Sprayed Ceramic Coatings, *Thin Solid Films,* Vol 112, 1984, p 89-95
20. C.J. Li and A. Ohmori, Relationships Between the Microstructure and Properties of Thermally Sprayed Deposits, *J. Thermal Spray Technol.,* Vol 11, 2002, p 365-374
21. S. Boirelavigne, C. Moreau, and R.G. Saintjacques, The Relationship Between the Microstructure and Thermal-Diffusivity of Plasma-Sprayed Tungsten Coatings, *J. Thermal Spray Technol.,* Vol 4, 1995, p 261-267
22. T.J. Lu and J.W. Hutchinson, Thermal-Conductivity and Expansion of Cross-Ply Composites with Matrix Cracks, *J. Mech. Phys. Solids,* Vol 43, 1995, p 1175-1198
23. D.Y. Tzou, The Effect of Internal Heat-Transfer in Cavities on the Overall Thermal-Conductivity, *Int. J. Heat Mass Transfer,* Vol 34, 1991, p 1839-1846
24. Z. Hashin, The Differential Scheme and Its Application to Cracked Materials, *J. Mech. Phys. Solids,* Vol 36, 1988, p 719-734
25. T.H. Bauer, A General Analytical Approach Toward the Thermal-Conductivity of Porous-Media, *Int. J. Heat Mass Transfer,* Vol 36, 1993, p 4181-4191
26. S. Raghavan, H. Wang, R.B. Dinwiddie, W.D. Porter, and M.J. Mayo, The Effect of Grain Size, Porosity and Yttria Content on the Thermal Conductivity of Nanocrystalline Zirconia, *Scripta Mater.,* Vol 39, 1998, p 1119-1125
27. K.S. Ravichandran, K. An, R.E. Dutton, and S.L. Semiatin, Thermal Conductivity of Plasma-Sprayed Monolithic and Multilayer Coatings of Alumina and Yttria-Stabilized Zirconia, *J. Am. Ceram. Soc.,* Vol 83, 1999, p 673-682
28. T.J. Lu, C.G. Levi, H.N.G. Wadley, and A.G. Evans, Distributed Porosity as a Control Parameter for Oxide Thermal Barriers made by Physical Vapor Deposition, *J. Am. Ceram. Soc.,* Vol 84, 2001, p 2937-2946
29. F.P. Incropera and D.P. Dewitt, *Introduction to Heat Transfer,* John Wiley & Sons, 1996
30. A.C. Fox and T.W. Clyne, The Gas Permeability of Plasma Sprayed Ceramic Coatings, *Thermal Spray: A United Forum for Scientific and Technological Advances,* C.C. Berndt, Ed., Sept. 15-18, 1997 (Indianapolis, IN), ASM International, 1998, p 483-490
31. D.W. Lee and W.D. Kingery, Radiation Energy Transfer and Thermal Conductivity of Ceramic Oxides, *J. Am. Ceram. Soc.,* Vol 43, 1960, p 594-605
32. J.G. Peelen and R. Metselaar, Light Scattering by Pores in Polycrystalline Materials: Transmission Properties of Alumina, *J. Appl. Phys.,* Vol 45, 1974, p 216-220
33. J. Manara, R. Caps, F. Raether, and J. Fricke, Characterization of the Pore Structure of Alumina Ceramics by Diffuse Radiation Propagation in the Near Infrared, *Opt. Commun.,* Vol 168, 1999, p 237-250
34. R. Siegel and J.R. Howell, *Thermal Radiation Heat Transfer,* McGraw-Hill, New York, 1972
35. T. Makino, T. Kunitomo, I. Sakai, and H. Kinoshita, *Thermal Radiation Properties of Ceramic Materials, Heat Transfer. Jap. Res.,* Vol 13, 1984, p 33-50
36. F. Cabannes and D. Billard, Measurement of Infrared-Absorption of Some Oxides in Connection with the Radiative-Transfer in Porous and Fibrous Materials, *Int. J. Thermophys.,* Vol 8, 1987, p 97-118
37. R. Siegel, Transient Thermal Analysis of a Translucent Thermal Barrier Coating on a Metal Wall, *J. Heat Transfer,* Vol 121, 1999, p 478-481
38. D.R. Clarke, Materials Selection Guidelines for Low Thermal Conductivity Barrier Coatings, *Surf. Coat. Technol.,* Vol 163-164, 2003, p 67-74
39. A.S. Samarskii and P.N. Vabishevich, *Computational Heat Transfer,* Vol 1, *Mathematical Modelling,* Wiley, Chichester, UK, 1995
40. J.C. Tannehill, D.A. Anderson, and R.H. Pletcher, *Computational Fluid Mechanics and Heat Transfer,* Taylor & Francis, Washington, D.C., 1997
41. J. Ilavsky, A.J. Allen, G.G. Long, S. Krueger, C.C. Berndt, and H. Herman, Influence of Spray Angle on the Pore and Crack Microstructure of Plasma-Sprayed Deposits, *J. Am. Ceram. Soc.,* Vol 80, 1997, p 733-742
42. A.J. Allen, J. Ilavsky, G.G. Long, J.S. Wallace, C.C. Berndt, and H. Herman, Microstructural Characterization of Yttria-Stabilized Zirconia Plasma-Sprayed Deposits Using Multiple Small-Angle Neutron Scattering, *Acta Mater.,* Vol 49, 2001, p 1661-1675
43. A. Kulkarni, Z. Wang, T. Nakamura, S. Sampath, A. Goland, H. Herman, J. Allen, J. Ilavsky, G. Long, J. Frahm, and R.W. Steinbrech, Comprehensive Microstructural Characterization and Predictive Property Modeling of Plasma-Sprayed Zirconia Coatings, *Acta Mater.,* Vol 51, 2003, p 2457-2475
44. H. Boukari, A.J. Allen, G.G. Long, J. Ilavsky, J.S. Wallace, C.C. Berndt, and H. Herman, Small-Angle Neutron Scattering Study of the Role of Feedstock Particle Size on the Microstructural Behavior of Plasma-Sprayed Yttria-Stabilized Zirconia Deposits, *J. Mater. Res.,* Vol 18, 2003, p 624-634
45. G. Trapaga, E.F. Matthys, J.J. Valencia, and J. Szekely, Fluid Flow, Heat Transfer and Solidification of Molten Metal Droplets Impinging on Substrates; Comparison of Numerical and Experimental Results, *Metall. Trans.,* Vol 23B, 1992, p 701-718
46. H. Zhang, Theoretical Analysis of Spreading and Solidification of Molten Droplet During Thermal Spray Deposition, *Int. J. Heat Mass Transfer,* Vol 42, 1999, p 2499-2508
47. T. Bennett and D. Poulikakos, Splat-Quench Solidification: Estimating the Maximum Spreading of a Droplet Impacting a Solid Surface, *J. Mater. Sci.,* Vol 28, 1993, p 963-970
48. R. McPherson, A Review of Microstructure and Properties of Plasma Sprayed Ceramics Coatings, *Surf. Coat. Technol.,* Vol 39/40, 1989, p 173-181
49. D.M. Zhu and R.A. Miller, Sintering and Creep Behaviour of Plasma-Sprayed Zirconia- and Hafnia-Based Thermal Barrier Coatings, *Surf. Coat. Technol.,* Vol 109, 1998, p 114-120